AAOL Wavefront Data Reduction Approaches

Shaddy Abado*[a], Stanislav Gordeyev[a], Eric Jumper[a]

[a]Institute for Flow Physics and Control, University of Notre Dame, Notre Dame, IN, 46556

ABSTRACT

This paper addresses a method for extracting the convection speed and direction of aberrations present in wavefronts due to aero-optical turbulence over the pupil of a turret on the side of an airborne platform. The method is applied to data from the Airborne Aero-Optics Laboratory (AAOL). Such convection information is useful in designing feed-forward adaptive-optic approaches. The method makes use of a four-beam Malley probe technique derived by constructing a two-dimensional local convective velocity-distribution over the beam's aperture. This technique is based on extending the analysis of the Notre-Dame-developed Malley probe. Two wavefront datasets (Azimuth 157° and Elevation 40°; Azimuth 42° and Elevation 43°) from the AAOL are analyzed using the derived method, the first where the laser propagates through fully-separated flow and the second where the laser propagates through an attached-flow region. Finally, the two-dimensional Proper Orthogonal Decomposition is applied to one in-flight measured dataset to determine the spatial requirements of deformable mirrors in an adaptive-optics system. The paper concludes with a discussion that points out the usefulness of the two-dimensional velocity-distributions in characterizing the various flow structures which convect over the aperture.

Keywords: Aero-optics, Adaptive-optics, Malley Probe, Four-beam Malley Probe, Proper Orthogonal Decomposition, Airborne Aero-Optics Laboratory, Hemisphere-on-Cylinder Turret, Flat Windowed Turret

1. INTRODUCTION

As discussed in detail elsewhere [1], aero-optics refers to the aberrations imposed on an otherwise-planar wavefront of a laser propagated through near-filed turbulence in flows over and around a turret on an airborne laser platform. The magnitude of these aberrations can be quite large depending on the flight altitude and Mach number as well as the pointing direction in azimuth (Az) and elevation (El) of the outgoing beam, referenced to the angle of the flight relative wind (i.e., Az 0.0^o, El 0.0^o being directly into the flight direction) [2]. The magnitude of these aberrations can be sufficiently large to greatly reduce the system's useful field of regard. In addition to the aero-optic aberrations, aero-buffet causes line-of-sight jitter which appears on the wavefront as tip-tilt. While some of the tip-tilt on the wavefront is due to aero-optics, by far the largest component is due to aero-buffet. For the purpose of this paper, we will assume that a fast-steering mirror of sufficient bandwidth is able to remove the tip-tilt and from here on we will discuss only the higher-order aberrations after tip-tilt has been removed.

Adaptive-optics, which attempts to place a conjugate wavefront on the beam before it propagates through the turbulence [3], could theoretically reopen the field of regard; however, both the spatial and temporal frequencies contained in the aberrations make conventional adaptive-optic approaches minimally effective and often cause worse aberrations than are present with no "correction." Over the past half-decade, progress in developing feed-forward techniques to overcome adaptive-optic-system latencies have been proposed and in some cases successfully demonstrated; however, these techniques rely on *a priori* knowledge of the character of the disturbances obtained in one way or another that may involve "training" the control system [4,5].

These feed-forward approaches take advantage of the fact that, while the aberrations evolve as they pass over the aperture, they can be treated over short periods of time as being frozen and "convect." As such, knowledge of the local speed and direction of aberrations as a function of location over the aperture are particularly relevant in shaping the feed-forward, adaptive-optic approaches.

With the advent of copious, time-resolved, in-flight wavefront data from the Airborne Aero-Optics Laboratory (AAOL) [6], new techniques for analyzing and manipulating wavefronts have been developed. References [5, 7-8] discuss some of the new methods being developed; this paper discusses additional analysis techniques that begin with determining the convective speed and direction of the aberration as functions of aperture location, azimuth and elevation, and flight conditions.

---

*Corresponding author, E-mail: sabado@nd.edu

The approach presented here for estimating the local convective velocity involves treating the sub-apertures on the wavefronts, which are from Shack-Hartmann sensors, as individual wavefront slope data and extending the analysis we use for the Notre-Dame-developed Malley probe. A Malley probe is a technique used to infer wavefront statistics by using two small beams projected through the turbulence at various locations over a would-be aperture. In order to properly describe our analysis technique, we will first give an brief overview of the Malley probe analysis technique and then generalize that first to a four-beam Malley probe and then to analyzing wavefronts. Finally the technique will be applied to some of the AAOL data as an example of its use.

2. ANALYSIS TECHNIQUE

2.1 Malley Probe Basics

The Malley probe is named after Michael Malley who first recognized that aberrations placed on a wavefront due to a laser beam being projected through fluid turbulent structures that are convecting with the fluid will themselves convect through the aperture [9]. Notre Dame expanded on the method by, among other things, adding a second beam and developing analysis techniques for interpreting the Malley probe data; details on the sensor can be found elsewhere [1,10,11], but they are given in brief here.

As a first order approximation, it can be assumed that the turbulence intrinsic time scale is longer than its passing time. Based on this, the turbulent flow can be thought of as simply convecting at a constant mean velocity, U_c, without evolution; this approximation is often referred to as the Taylor's frozen-flow hypothesis, and the turbulent flow is said to be "frozen"[12]. If a single-point measurement is performed along the flow line that is convecting at velocity U_c, then the time correlations at time delay τ is directly related to the spatial correlations at separation ($\tau \cdot U_c$) in the direction of the mean flow. Taylor's frozen-flow hypothesis allows for the spatial frequency, k, to be obtained from the temporal frequency, ω, such that

$$k = \frac{\omega}{U_c} \tag{1}$$

Hence, the temporal data from a single sensor measurement location can be used to infer information about the spatial structure of turbulence, and vice versa. Invoking Taylor's frozen-flow hypothesis allowed Malley, *et al.* [9] to develop a single, small-diameter (1 – 3 mm) laser-beam instrument which provides a measurement of the Optical Path Difference (OPD) variance as a function of spatial frequency if the convection velocity is known; in their case they inferred the velocity by use of hot wires.

Using Huygens' principle, which states that a ray of light travels normal to its associated optical wavefront [3], it is possible to relate the beam deflection angle, θ_x, to the derivative in the convection direction of a would-be, larger-aperture wavefront, W, at the location of the probe beam, such that

$$\theta_x(t, x, y) = \frac{dW(t, x, y)}{dx} \tag{2}$$

assuming small θ_x. Similarly, in the y-direction, θ_y can be found as the derivative of $W(t, x, y)$ with respect to y.

If Taylor's frozen-flow hypothesis is also invoked, then it is possible to relate space and time through the convective velocity of the optically-active structures. Applying this hypothesis to Eq. (2), then it is possible to re-write it as,

$$\theta_x(t, x, y) = \frac{1}{U_c} \frac{dW(t, x, y)}{dt} \tag{3}$$

Integrating Eq. (3) with respect to t at the fixed point (x_0, y_0) and recalling that the optical path difference, OPD, is the conjugate of the wavefront, then Eq.(3) can be expressed as

$$OPD(t, x_0, y_0) = -U_c \int_0^t \theta_x(t, x_0, y_0) dt \tag{4}$$

To overcome the limitation imposed by having to use hot wires to obtain U_c, Notre Dame added an additional closely-spaced beam just downstream of the first beam. Since Taylor's frozen-flow hypothesis is used, the time series recorded from the downstream beam jitter, θ_1, should be identical to the time series from the upstream beam jitter, θ_2, except shifted in time. The time correlation of the two jitter signals allows the estimation of U_c. Such a two-beam instrument is referred to as Malley probe [10]. A schematic of basic Malley probe setup is shown in Figure 1.
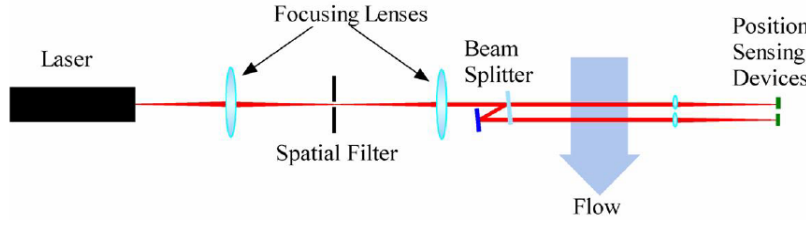

Figure 1. Schematic of basic Malley probe setup [13].

Two main methods exist to evaluate the covection speed of the aberrations caused by the flow structures: a *direct method* and a *spectral method*. A detailed derivation of each method can be found in Reference [11]. Here, a short description of both methods is provided.

In both methods, the convection speed is calculated based on the equation

$$U_c = \frac{\Delta}{\tau_{max}} \tag{5}$$

where, Δ is the known beam separation distance, and τ_{max} is the maximum time delay between the two jitter signals θ_1 and θ_2.

In the *direct method*, the time delay is related to the maximum correlation time of the two jitter signals, which is calculated as,

$$R(\tau) = corr\{\theta_1(t) \times \theta_2(t + \tau)\} \tag{6}$$

where τ is the correlation time. The use of the *direct method* showed that it was sensitive to contamination in the deflection signals due to vibration and electronic noise. This led to the development of the *spectral method*, the basis of which is illustrated in Figure 2.

In the *spectral method*, the time delay can be found as a function of frequency, $\dfrac{\Delta\phi}{\Delta f} = \dfrac{2\pi \cdot \dfrac{\tau}{T_2} - 2\pi \cdot \dfrac{\tau}{T_1}}{\dfrac{1}{T_2} - \dfrac{1}{T_1}} =$, so

that $\tau = \dfrac{\Delta\phi}{\Delta f} \cdot \dfrac{1}{2\pi}$ and finally $U_c = \dfrac{\Delta}{\tau_{max}}$. This can be done by using the argument of the cross correlation as:

$$\tau_{max}(f) = \frac{1}{2\pi} \frac{d}{df} \arg[S(f)] \tag{7}$$

where $S(f)$ is the ensemble-averaged spectral cross-correlation function which is defined as:

$$S(\omega) = \frac{1}{T} \langle \hat{\theta}_1(\omega), \hat{\theta}_2^*(\omega) \rangle \tag{8}$$

here, $\langle \cdot \rangle$ denotes the ensemble averaging, $\hat{\theta}$ denotes to the Fourier transform, $*$ denotes the complex conjugate, and T is a block sampling time. $S(\omega)$ represents the phase angle between the two signals for frequency f. This makes the *spectral method* particularly suitable to flow caused aberrations, which are characterized with different structure sizes because each flow will be predominantly optically active in only a certain frequency bandwidth, enabling us to calculate the convective velocity as function of frequency; thus Eq. (5) can be re-written as,

$$U_c(f) = \frac{\Delta}{\tau_{\max}(f)} \tag{9}$$
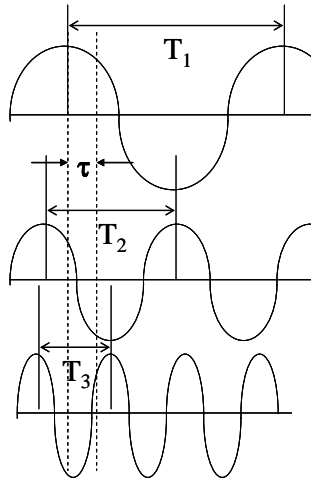
For a fixed time delay, t, the phase shift for different periods is:

$$\phi_i = \frac{\tau}{T_i} 2\pi$$

The frequency for a given period is:

$$f_i = \frac{1}{T_i}$$

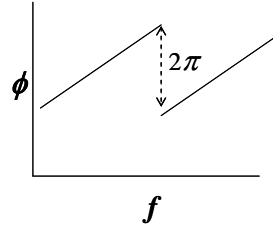**If f is plotted vs ϕ then we would get a straight line**

Figure 2. Illustration of the basis for the *spectral method*.

2.2 Extension of the Two-Beam Malley Probe to Four Beams

As discussed above, the Malley probe principle of operation is based on the assumption that the optical aberrations are 'frozen' and at least sufficient knowledge of the convection direction is known to align the two beams in the streamwise direction. Over a full aperture aberrations will evolve, in general, and it is likely that the convection speed and direction will change at different locations over the aperture. These complications can be overcome by using a two-dimensional array of detectors to investigate a large aperture. Rather than using individual beams, a Shack-Hartmann wavefront sensor [3] can be used by treating each sensor's lenslet as a separate beam of the sub-aperture size, where the deflection angle over each sub-aperture represents the average wavefront local tilt. Based on this, each beam's sub-aperture represents a 'probe-beam' which is propagating through the flow-field, hence, a two-dimensional array of Malley probes. The main advantage of this multiple-beam instrument is that with an entire array of probes, the evolution of a structure as it convects across adjacent sub-apertures will be sufficiently slight that it can be treated as 'frozen' between adjacent sub-apertures. Furthermore, different convection velocities will be obtained at the same location depending on which two adjacent sub-apertures are used. The true magnitude and direction of the aberration convection can then be found by vector summing of the inferred velocity from each pair in a square array if the sub-apertures are layed out in an equidistant rectilinear array; the lenslet arrays used on AAOL are of this type. In this array pattern, the x- and y-directions define the array so that adjacent correlations in the x-direction will yield local velocity components in the x-direction, U_x, and in the y-direction, U_y, then both local wavefront gradients may be used to calculate $U_c^{Local}(x, y)$ as

$$\vec{U}_c(x, y) = U_x \hat{x} + U_y \hat{y} \tag{10}$$

Based on this, the local convective velocity angle across the cell, α, can be expressed as,

$$\alpha = \tan^{-1}\left(\frac{U_y}{U_x}\right) \tag{11}$$

For a rectangular lenslet array, four adjacent sub-apertures can be used to form a rectangular four-beam cell. An example layout of such a cell is shown in Figure 3 (left). Here, the four probe-beams at the corners of the cell define a *four-beam Malley probe* instrument. Rather than just two correlation opportunities, notice that the four-beam Malley probe actually has 6 cross-correlation possibilities, see Figure 3 (right).
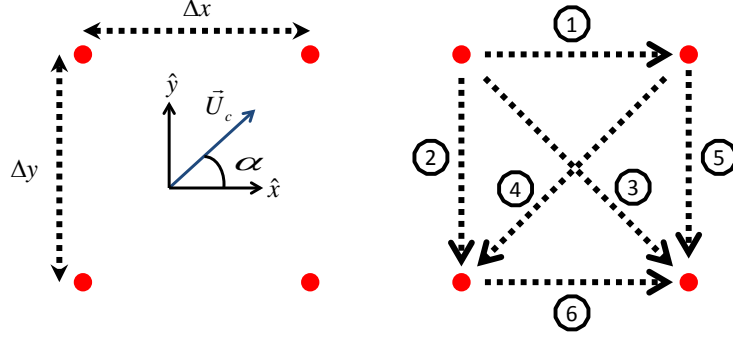

Figure 3 (left) Four-beam Malley probe layout; (right) Six possible Malley probe combinations.

If a structure is covecting at velocity $\vec{U}_c$ between two detectors at a distance $\vec{d}_{i,j}$ (see Figure 4), then the direction of convection can be represented as,

$$\hat{n} = \frac{\vec{U}_c}{\left\|\vec{U}_c\right\|} \tag{12}$$

and the convection time it takes for the structure to convect through this distance can be calculated as

$$\tau_i = \frac{\hat{n}\cdot\vec{d}_i}{\left\|\vec{U}_c\right\|} = \frac{\vec{U}_c\cdot\vec{d}_i}{\left\|\vec{U}_c\right\|^2} \tag{13}$$
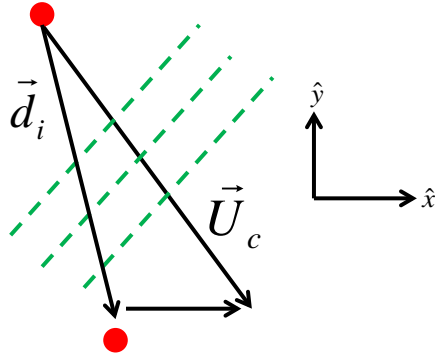

Figure 4. Schematic of a convecting structure.

Defining two parameters u and v as:

$$u = \frac{U_x}{U_x^2 + U_y^2} \tag{14}$$

and

$$v = \frac{U_y}{U_x^2 + U_y^2} \qquad (15)$$

Then for all 6 possible correlations, an over-determined system of equations with 6 equations and 2 unknowns can be defined:

$$\begin{bmatrix} \Delta x & 0 \\ 0 & -\Delta y \\ \Delta x & -\Delta y \\ -\Delta x & -\Delta y \\ 0 & -\Delta y \\ \Delta x & 0 \end{bmatrix} = \begin{bmatrix} u \\ v \end{bmatrix} \cdot \begin{bmatrix} \tau_1 \\ \tau_2 \\ \tau_3 \\ \tau_4 \\ \tau_5 \\ \tau_6 \end{bmatrix} \qquad (16)$$

here $\tau_i \ (i = 1 \ldots 6)$ are the time delays of all Malley probe combination, and can be calculated based on the *spectral method* described in the previous section. This system of equations can be re-written as,

$$A\vec{x} - \vec{b} = \vec{0} \qquad (17)$$

where, A denotes the displacement matrix in Eq. (16), while $\vec{x}$ and $\vec{b}$ denote the velocity and time delays vectors in Eq. (16), respectively.

The over-determined system of equations given above can be solved in a least squares sense to find u and v. The local velocity components in the x- and y-directions can be expressed as,

$$U_x = \frac{u}{u^2 + v^2} \qquad (18)$$

and

$$U_y = \frac{v}{u^2 + v^2} \qquad (19)$$

While the local convective velocity magnitude is expressed as,

$$U_c = \sqrt[2]{U_x^2 + U_y^2} \qquad (20)$$

To achieve a spatial mapping of the local convective velocities across the aperture, the analysis described above can be repeated at every possible combination of four sub-apertures across the entire beam's aperture.

Prior to applying the derived four-beam Malley probe analysis to the AAOL in-flight measured data, it should be emphasized that the solution of Eq. (16) is not an exact solution, but rather it is a solution that finds $\vec{x}$ which minimizes the length of $A\vec{x} - \vec{b}$ as much as possible. The over-determined system of equations in Eq. (16) allow us to ignore Malley probe combinations which do not provide good results due to various sources of errors and reduce experimental noise.

3. APPLICATION OF THE TECHNIQUE TO AAOL DATA

The technique described in the previous section can be applied to the time series of wavefronts on all of the AAOL data, but as an example of its application, two particular datasets will be used. The first dataset is somewhat backward looking direction with azimuth and elevation of 157° and 40°, respectively. For this pointing direction, a dataset of wavefronts for a flight at $15 \, kft$ altitude and a Mach number of 0.4 was chosen. This viewing angle represents a case where the flow is separated behind the turret and is dominated by the large coherent structures of the shear layer. At $15 \, kft$ the air density was $\sim 0.7 \, kg/m^3$, and the speed of sound was $\sim 322 \, m/s$ so that the freestream velocity was $\sim 129 \, m/s$. The

wavefront data was collected with high-speed Shack-Hartmann wavefront sensor framing at $20\,kHz$ and the dataset contained 9189 frames of $30x29$ sub-apertures laid out in a rectangular array.

It is common to present wavefront results in non-dimensional quantities for easy scaling to any relevant flight conditions and turret configurations different than those experienced during the in-flight data collection. As such, the OPD, spatial frequency, and temporal frequency were non-dimensionalized similar to the scaling laws proposed in Reference [14].

3.1 Spectral Analysis

The temporal spectral content of the in-flight measured wavefronts can be estimated by calculating the power spectral density (PSD) of each sub-aperture and then averaging over the entire aperture (578 sub-apertures). To assure that each sub-aperture's PSD has the same weight on the aperture-averaged PSD, each sub-aperture OPD signal was normalized by its time averaged, root-mean-squares value, $OPD_{rms|Sub}^{ND}$. The PSD's of all sub-apertures and the aperture-averaged PSD as a function of non-dimensional temporal frequency are presented in Figure 5. It can be seen that the individual sub-apertures PSD distribution (dots) resembles the aperture-averaged PSD curve (solid line).

The most notable features of the PSD are the broad-band hump with a peak value near non-dimensional frequency of 1.02 and the sharp spike at a non-dimensional frequency of 8.34. The existence of a broad-band hump in the PSD indicates the presence of large-scale coherent structures due to the presence of a shear layer. This shear layer develops from the separation point on the turret and dominates the separated flow at large aft-looking viewing angles, similar to the angle presented for this first example. It can be assumed that the source of the sharp peak is different than the shear layer due to its sharpness compared to the broad-band hump. In addition to the shear layer broad-band hump and the sharp spike, it can also be seen that for large frequencies, the PSD of the optical distortions roll-off at a $-\frac{4}{3}$ rate (dashed line). This PSD roll-off rate is an indication of the difference between aero-optics and atmospheric propagation [1] where for atmospheric propagation, high-frequency optical aberrations caused by the transport of passive scalars would show a PSD roll-off of a $-\frac{2}{3}$ rate [21].
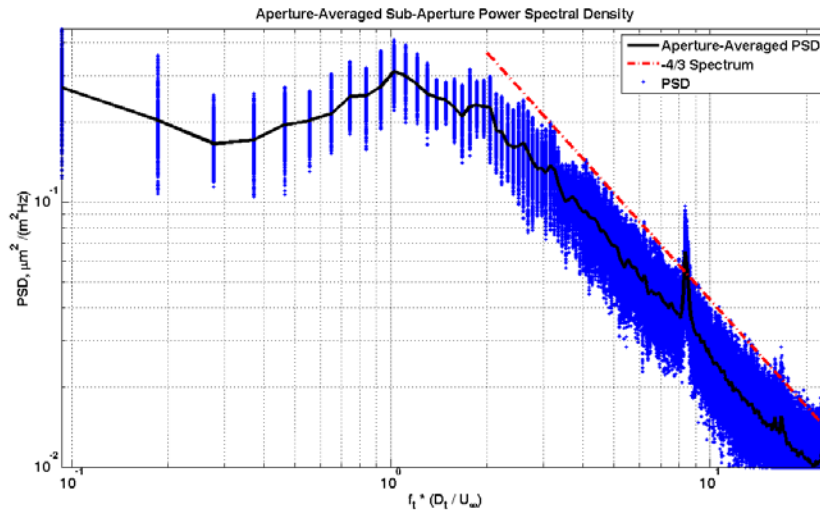

Figure 5. Aperture-averaged sub-aperture Power Spectral Density versus a non-dimensionalized temporal frequency for Az and El of 157° and 40°, respectively, D_t denotes the turret's diameter and U_∞ denotes the freestream velocity.

3.2 Velocity Mapping for Az 157° and El of 40°

A mapping of the local convective velocity across the beam's aperture can be constructed as discussed in section 2.2. This mapping can be performed by defining four-beam Malley probe cells and calculating the spectral cross-correlation of the 6 possible signal combinations in each four-beam Malley probe. The over-determined system of equations with 6 equations and 2 unknowns is then solved to determine the local phase convective velocity in each four-beam Malley

probe. For the dataset presented here, 498 possible four-beam Malley probes were defined to map the local phase convective velocity across the beam's aperture for the Az 157° and El of 40° case.

Spectral cross-correlation phase versus frequency plots of one of the four-beam Malley probe cells are shown in Figure 6. In this figure, each plot represents the spectral cross-correlation phase of a different signal combination (the number in the parenthesis). For convenience, the phase plots were plotted versus a dimensional temporal frequency; however, if needed, the plots can also be plotted versus a non-dimensional temporal frequency.
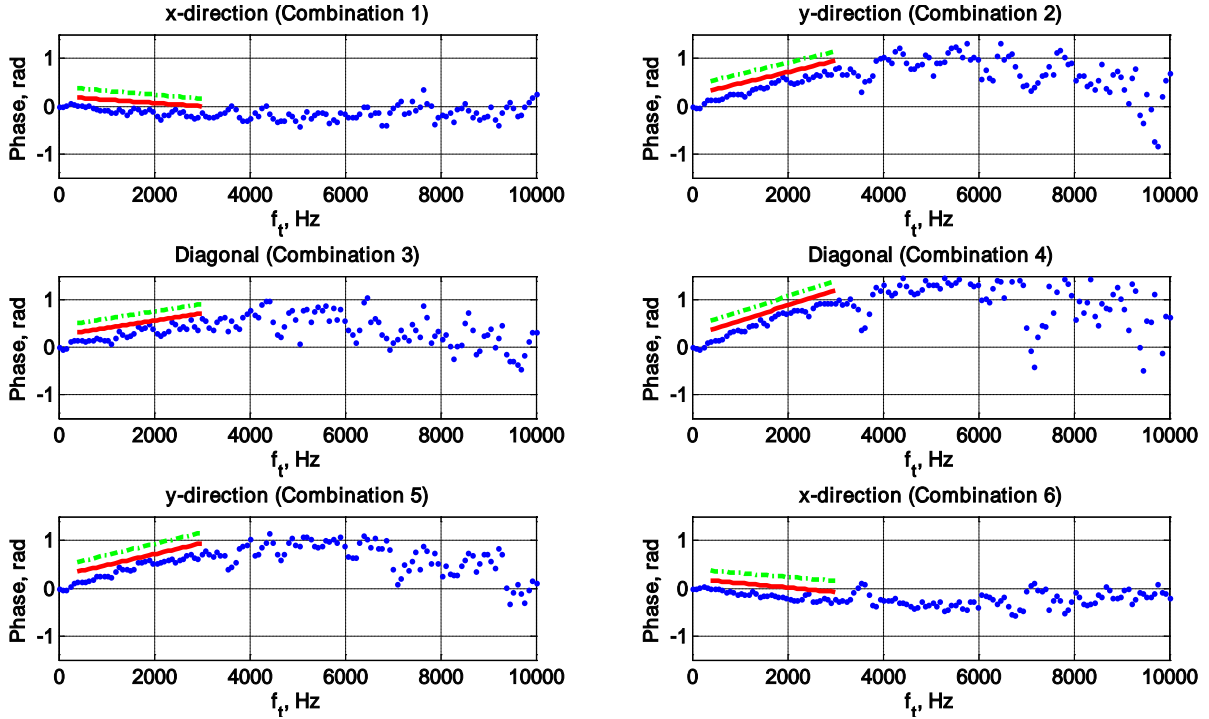

Figure 6. Six spectral cross-correlation phase plots of a random four-beam Malley probe. Linear fit (solid line); approximated velocity (dashed line).

Different temporal frequency ranges were tested to determine the optimal frequency range at which the time delay of each cross-correlation should be calculated. Based on the six plots in Figure 6, it can be generally concluded that for temporal frequencies smaller than $400\,Hz$, the spectral cross-correlation phase is approximately zero. This observation indicates that jitter data below $400\,Hz$ are due to unsteady but stationary effects such as vibrations and unsteady but stationary aerodynamic lensing, and no convicting structures can be unfolded and studied for this frequency range. Similarly, for frequencies larger than $3000\,Hz$, the phase plots are contaminated by noise and do not exhibit a linear phase characteristic which is expected in the *spectral method*, see Figure 2. It can be seen that over the range of frequencies corresponding to the broad-band hump seen in Figure 5, the slope of the spectral cross-correlation phase curve is nonzero and takes a form that can be approximated as a linear line. As was shown in Eqs. (7) and (9) and Figure 2, the slope of this linear line can be used to compute the phase convective velocity. Based on this, it was determined that linear lines least-squares fits at a $400\text{-}3000\,Hz$ frequency range give the best results (solids lines in Figure 6). These slope values were converted into time delays based on Eq. (7) and substituted into Eq. (16) to solve for u and v in a least-squares sense. To verify that the least-squares solutions of Eq. (16) are indeed accurate, the time delay values were re-calculated based on $A\vec{x}$, and the phase slopes were found based on Eq.(7). The new phase curves were plotted again on each phase plot (dashed lines in Figure 6). It can be seen that the slopes of the dashed lines are nearly identical to the slopes of the solid lines. This indicates that the least-squares solutions of the over-determined system of equations are indeed resolving the correct u and v values which are measured by the six spectral cross-correlation phase plots.
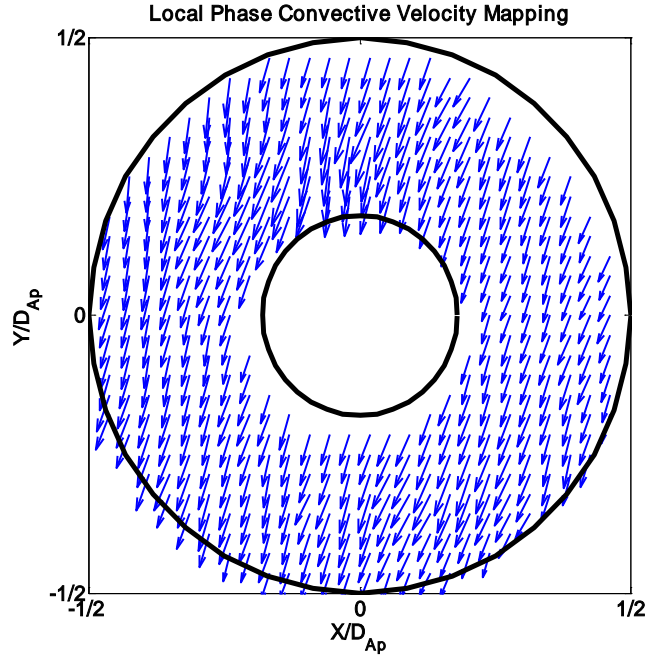
Figure 7. Local phase convective velocity mapping for the Az 157° and El of 40° case.

Based on these analyses, at each four-beam Malley probe cell, local convection velocity mapping was performed and is presented in Figure 7. It can be seen that the flow is convecting in a uniform direction with a slight negative angle with respect to the negative y-axis. Recall that the x- and y-axes denote the axes of the wavefront sensor and not the streamwise and spanwise directions of the flow-field. Both axes are normalized by the AAOL's turret aperture, D_{Ap}.

The local phase convective velocity mapping in Figure 7 is, although somewhat different in magnitude and direction, representative of the flow characteristics at the larger aft-looking viewing angles obtained for the flight on which this dataset was taken and, in fact, representative of data from other flights for similar aft-looking angles but at different altitudes and Mach numbers up to Mach 0.55. At these aft-looking angles the flow-field is dominated by large, convecting, coherent structures that form in the shear layer [15]. These dominant coherent structures explain the uniformity of the velocity mapping. At other viewing angles when local structures might exist in the flow-field, such as local separation bubbles, this mapping uniformity breaks down and regions of different flow directions appear in the velocity mapping. A mean local convective velocity of $\overline{U}_c^{Local} \sim 106.1 \pm 14.8 \, ^m\!/\!_s$, and a mean local convective angle of

$\overline{\alpha}_c^{Local} \sim 71.7° \pm 4.9°$ with respect to the negative x-axis were calculated for the Az 157° and El of 40° case. The mean local convective velocity is 0.8 of the freestream velocity indicating that at this Mach number of 0.4, the flow accelerates around the turret, but remains fully subsonic. A similar value was reported by Gordeyev *et al.* [10,11], and when properly non-dimensionalized, the flow patterns at similar viewing angles are virtually identical as long as the flight Mach number remains below Mach 0.55; above Mach 0.55, the flow becomes transonic over the turret and the similarity begins to break down [16]. The small errors in estimating the $\overline{U}_c^{Local}$ and $\overline{\alpha}_c^{Local}$ values are additional indications of the uniformity of the flow.

3.3 Limitations and Inaccuracies of the Velocity Mapping

Despite the general trend of the local phase convective velocity direction and the small uncertainties in U_c^{Local} and α_c^{Local} values for the Az 157° and El of 40° case, the local phase convective velocity mapping has inaccuracies. These inaccuracies are meanly due to the limited numbers of data points available to perform ensemble averaging when calculating the PSD, in addition to the sensitivity of the phase convective velocity calculation to the frequency range at

which a linear line is fitted. Here, the ensemble average was performed over 35 data blocks of 2^8 data points each. These values were determined to be the optimal values for the trade-off between sufficient temporal frequency resolution and noise rejection. In addition, it was assumed here that the flow was convecting at the same frequency range in all six possible cross-correlations and in all 498 possible four-beam Malley probe combinations; this is not always the case. Therefore, the results presented in this section represent a general average case of U_c^{Local} and α_c^{Local} values.

To estimate the accuracy of the local phase velocity mapping as in Figure 7, and identify regions of potential errors, three diverging errors can be defined. These three diverging errors are: diverging error from the mean value of the local convective velocity in x-direction, $Error_x$, from the mean value of the local convective velocity in y-direction, $Error_y$, and from the mean value of the local convective angle, $Error_\alpha$. These three diverging errors can be expressed as,

$$Error_x = \left| U_x^{Local} - \overline{U}_x^{Local} \right| \tag{21}$$

$$Error_y = \left| U_y^{Local} - \overline{U}_y^{Local} \right| \tag{22}$$

and

$$Error_\alpha = \left| U_\alpha^{Local} - \overline{U}_\alpha^{Local} \right| \tag{23}$$

Contour plots of $Error_x$, $Error_y$, and $Error_\alpha$ are shown in Figure 8. The local phase convective velocity from Figure 7 is overlaid on the errors contour plots. It can be noticed that for the three contour plots the diverging errors are generally small, with respect to the local peak values. It also can be noticed that the diverging errors in the $Error_y$ contour plot are larger than the diverging errors in the $Error_x$ contour plot. This observation can be related to the fact that it was shown in Figure 7 that the flow-field structures convect in the y-direction, with a slight negative angle with respect to the negative y-axis. Therefore, it can be expected that the local convective velocity in the y-direction is larger than the local convective velocity in the x-direction, hence the larger error values. Based on the three contour plots in Figure 8, we can identify regions were the diverging errors match in the three plots. Such a region is marked with dashed circles in Figure 8. In this region, the $Error_y$ values exhibit a large peak in the diverging error value. This peak in $Error_y$ leads to a peak in $Error_\alpha$ value. It can be noticed that the local convective velocity in this region indeed exhibits a divergence from the uniform convective velocity mapping.
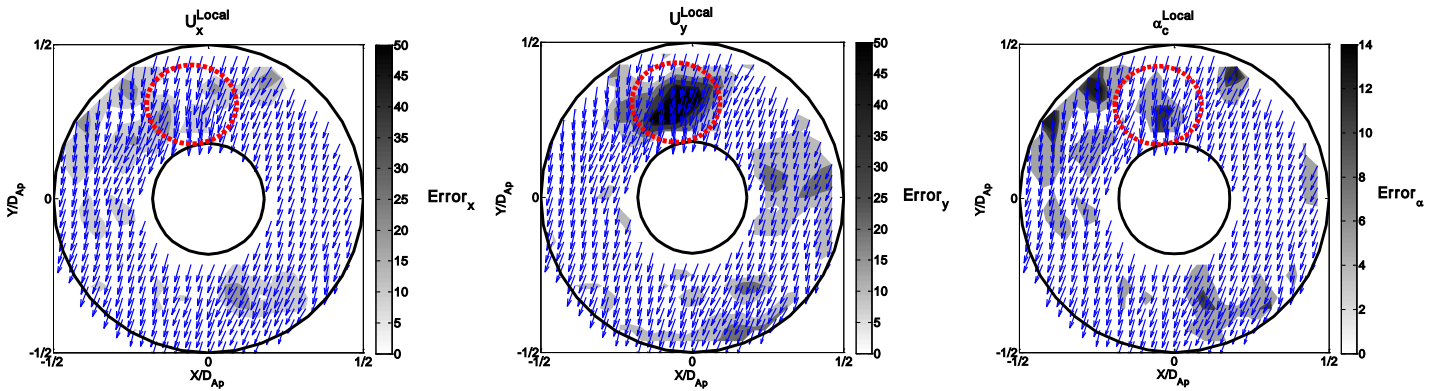

Figure 8. Contour plots of $Error_x$, $Error_y$, and $Error_\alpha$.

3.4 Velocity Mapping for Az 42° and El of 43°

An important point should be made here that for most aft-looking angles the structures causing most of the aberration on the wavefronts are convecting, as seen in Figure 7, and thus this example represents a good velocity mapping result. But, there are regions of the flow-field over the turret where the boundary layer is attached and the unsteady aberrations are due to unsteadiness in the overall aerodynamics of the flow around the turret caused by feed-forward of the unsteady

wake of the turret resulting in unsteady motion of the necklace vortex at the base of the turret [17]. In these forward-looking cases, the aberrations are unsteady but stationary, so attempts to obtain a velocity map fail. To demonstrate this, we will look at a second wavefront time series for a different flight at Mach 0.5 and $15\,kft$ and azimuth and elevation angles of 42° and 43°, respectively. If in fact the dominant aberrations are stationary, then the correlations for the four-bean Malley probes as in Figure 6 should yield the 6 possible phase plots that are approximately zero slope, i.e., no coherent structures are convecting across the aperture.

When the analysis technique is applied to the Az 42° and El of 43° case, this is what we find (see Figure 9). So, even though the four -beam Malley probe yields no convection velocities, it does yield useful information. In this case it tells us that the unsteadiness in the aberrations are due to stationary disturbances and not due to convected structures which are usually indicative of a separated flow.
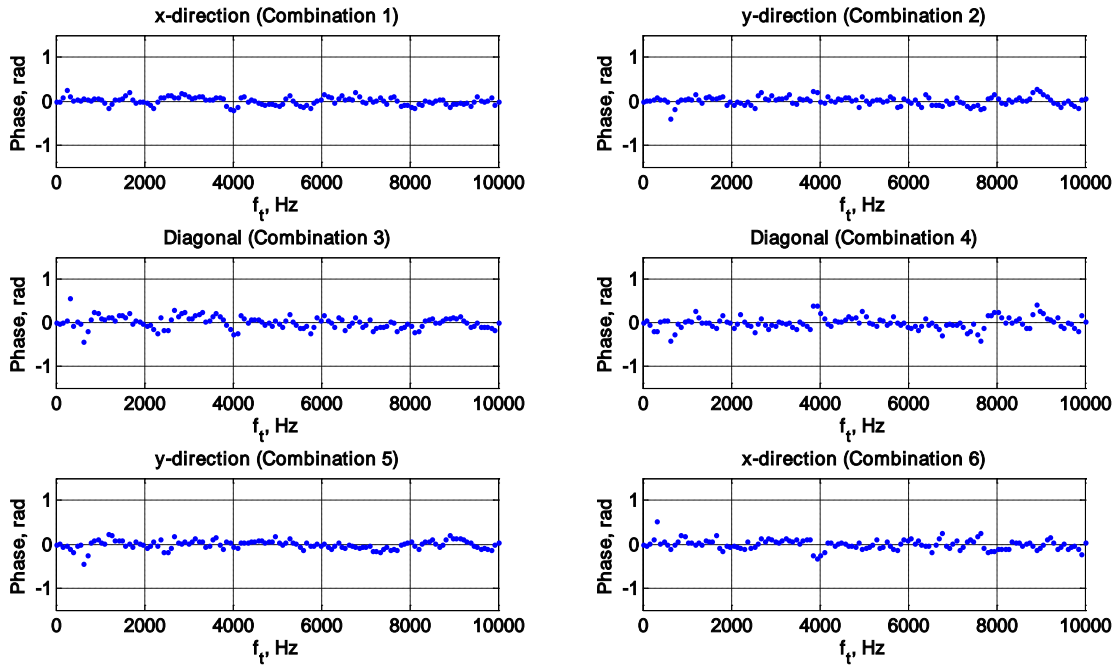

Figure 9. Six spectral cross-correlation phase plots of a random four-beam Malley probe for the Az 42° and El of 43° case.

4. PROPER ORTHOGONAL DECOMPOSITION ANALYSIS

In Reference [7], the use of Proper Orthogonal Decomposition (POD) was shown to be useful in determining spatial requirements of deformable mirrors (DM) in an adaptive-optics system. But once the velocity maps are determined, more specific requirements for DM's can be obtained. As discussed in Reference [7], the nice thing about using POD is that it separates the modal structures by their contribution to the overall aero-optical "energy" or OPD_{rms}^2, providing the quantitative measure of the aberrations due to that mode. As in Reference [7] two-dimensional POD techniques were applied to the in-flight measured wavefront datasets to characterize the flow-field around an airborne turret. A comprehensive discussion of the POD technique can be found in References [18]. The POD analysis splits the spatiotemporal field into a series of statistically-correlated, stationary, spatial patterns (spatial modes), $\varphi_i(x, y)$, and corresponding time-dependent coefficients (temporal coefficients), $a_i(t)$. This split simplifies the interpretation of the dominant wavefront structures and their characteristics. Views of the first 4 normalized spatial POD modes over the aperture for the first example are shown in Figure 10. The amount of "energy" contained in each specific mode (the 1st number in the parenthesis) and the cumulative "energy" up to that mode number (the 2nd number in the parenthesis) are given for each spatial POD mode. It can be seen that the higher the spatial POD mode-order, the higher the spatial

frequencies it contains. It should be noted that the ordinate of the spatial modes plots in Figure 10 are unitless; these modes do not actually represent OPD until they are multiplied by their associated temporal coefficients. The temporal coefficients of the first four POD modes for a time period of $10\,\mu s$ are shown in Figure 11. It can be seen that the overall amplitude of the temporal coefficients, and hence their relative contribution to the total "energy", decreases as the mode number increases.
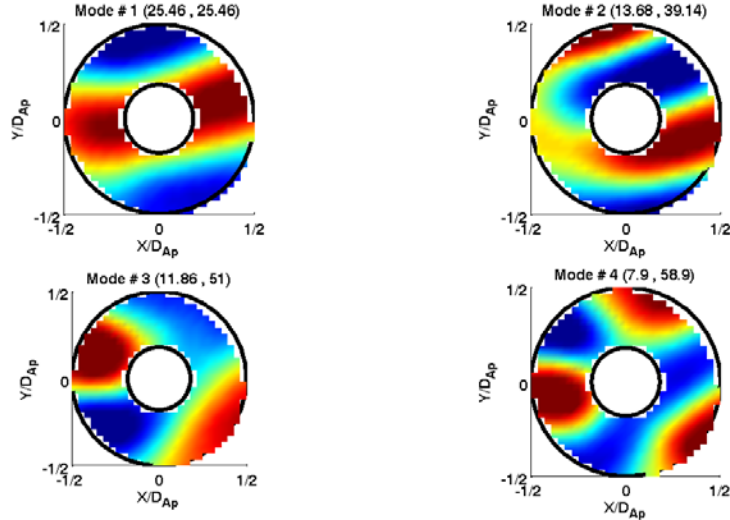

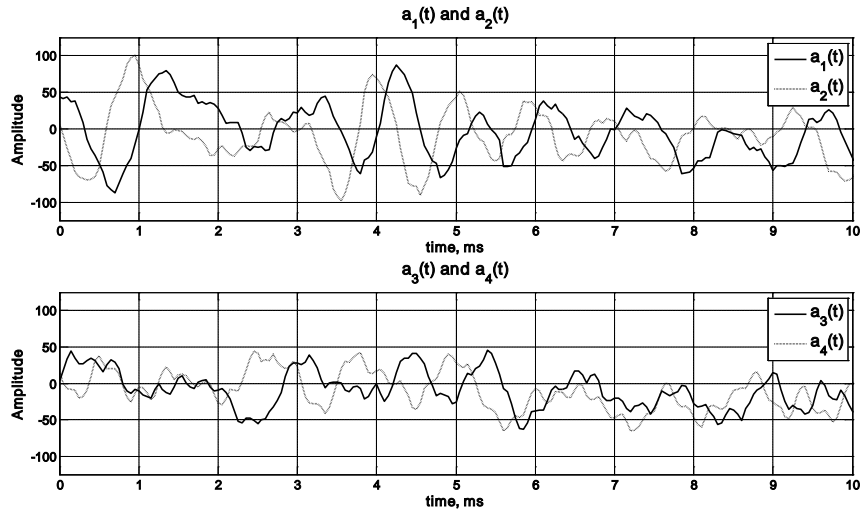Figure 10. Top view of the first 4 normalized spatial POD modes for the Az 157° and El of 40° case.

Figure 11. POD temporal coefficients of modes pairs for a time period of $10\,\mu s$.

As can be noticed in Figure 10, the spatial POD modes for the Az 157° and El of 40° case operate in pairs. That is, the first and second modes have similar form, but appear shifted in phase, similar to sine and cosine waves. A similar trend can be seen for the third and fourth modes, and so on. Similarly, it can also be seen in Figure 11 that the temporal coefficients $a_1(t)$ and $a_2(t)$ are almost identical in shape and frequency, except for a phase shift in time. A similar trend can also be seen for the temporal coefficients $a_3(t)$ and $a_4(t)$. This clearly suggests that the phase-shifted pairs represent propagating structures. The interaction between these spatial modes and temporal coefficients allows for the "motion" of the structures in the POD reconstruction. This "motion" occurs as each given mode shifts its temporal amplitude to its partner with subsequent time steps.

One of the defining characteristics of a shear layer is the presence of coherent vertical structures in the layer [15]. It is interesting to note that the first four spatial modes in Figure 10 are spanwise coherent and contain ~60% of the flow "energy". This result demonstrates that these four modes are due directly to the effect of the large, spanwise, coherent vertical structures of the shear layer. Furthermore, the convective nature of the shear layer can be demonstrated by the mode pairs in Figure 11.

So far, the analysis performed is essentially the same as in Reference [7]; however, with the knowledge from the velocity maps it is possible to obtain more specific spatial requirements in the flow and cross-flow directions. First, an average velocity over the entire aperture is obtained by averaging all of the velocity vectors in the map. Once done, the POD modes from Figure 10 can be reoriented as shown in Figure 12. Notice now that the spatial requirements for a DM will be very different in the streamwise direction (horizontal) and spanwise (vertical) directions. With the new orientation, correlation lengths of the POD modes can be computed in the new streamwise and spanwise directions.
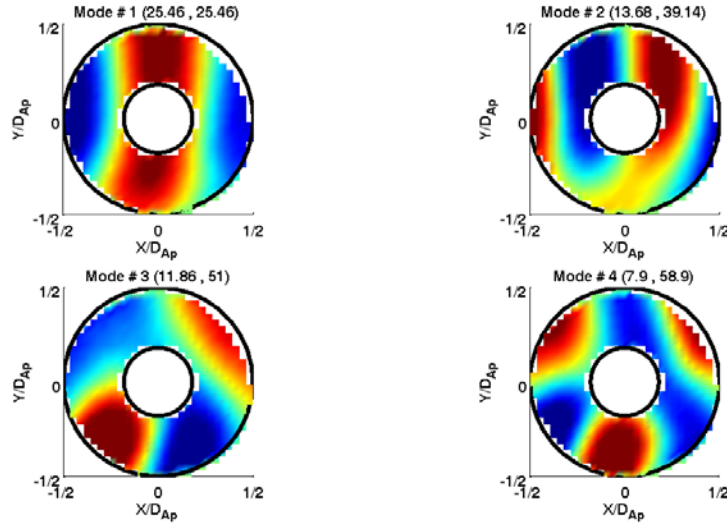

Figure 12. Reoriented POD modes from Figure 9 into the streamwise and spanwise directions given by the average convection velocity over the aperture.

A measure of the average size of the modal structures can be obtained from the two-dimensional, spatial, auto-correlation function of each spatial POD mode, now rotated into the streamwise and spanwise orientations. The two-dimensional, normalized, auto-correlating function can be defined as:

$$R(\Delta \vec{x}) = \frac{\langle \varphi(\vec{x}), \varphi(\vec{x} + \Delta \vec{x}) \rangle}{\langle \varphi(\vec{x}), \varphi(\vec{x}) \rangle} \tag{24}$$

Here, $\langle \cdot \rangle$ denotes the average operator and defined as $\int_{\Omega} \cdot \, d\vec{x}$, while $\Delta \vec{x}$ is the distance between two points on the POD spatial mode. $R(\Delta \vec{x})$ is a symmetric function of $\Delta \vec{x}$, with a maximum value equal to unity for $\Delta \vec{x} = \vec{0}$. It can be shown that the auto-correlation function of a periodic function is, itself, periodic with the same period. Therefore, the auto-correlation function can be used to identify periodicities in the observed physical signal, such as a coherent structure, which may be corrupted by random interference [19].

To characterize the spatial extent of the correlation, and therefore characterize the coherent structures, a *correlation length* is defined. The correlation length (which is often referred to as the *integral scale* in the context of turbulent flow) is defined as the distance in space beyond which physical events are uncorrelated [20]. The main advantage of defining a correlation length is that it provides a value for the size of the coherent structure. This value can be measured and compared between different coherent structures. Here we defined the correlation length as the location of the auto-correlation function's first minimum [10]. To fully characterize the two-dimensional coherent structures, both correlation

lengths in the streamwise and spanwise directions were calculated. If the large coherent structures are indeed convecting in the streamwise direction, then we should expect the coherent length in the streamwise direction to be the dominant correlation length.

Denoting the correlation length of the spatial POD mode n as $C.L.^n$, then its spatial frequency, f_s^n, can be defined as,

$$f_s^n = \frac{1}{C.L.^n} \tag{25}$$

and the number of periods of aberrations per aperture, $\frac{1}{Aperture}$, can be defined as

$$\frac{1}{Aperture} = D_{Ap} \cdot f_s^n \tag{26}$$

As it was mentioned earlier, and shown in the local phase velocity mapping in Figure 7, the x- and y-axes of the wavefront sensor are not aligned with the streamwise and spanwise directions of the flow-field; therefore, to appropriately evaluate the coherent lengths in the streamwise and spanwise directions, the POD modes of Figure 10 were aligned in the streamwise and spanwise orientation, as shown in Figure 12, prior to calculating its auto-correlation function. For each two-dimensional auto-correlation function, two correlation length values were evaluated based on one-dimensional slices in the streamwise and spanwise directions of the auto-correlation function.

To justify the necessity to rotate the spatial POD modes prior to calculating the auto-correlation function, a comparison between the number of periods of aberration per aperture, which are calculated based on the original (non-rotated), and the rotated spatial POD modes, is presented in Figure 13 for the first 200 POD modes. The spatial Nyquist frequency, which sets the spatial limit over the smallest structure size that can be resolved, and is also plotted (dashed line).
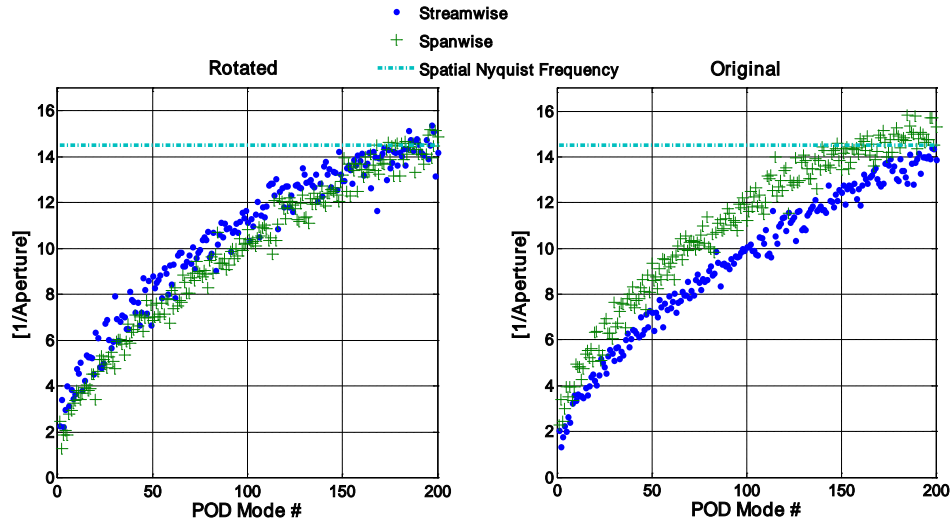

Figure 13. Comparing between the number of periods of aberration per aperture based on the definition of coherent length as the location of the first minimum of the auto-correlation function for the: (left) Rotated spatial POD modes; (right) Original spatial POD modes.

Based on Figure 13, it can be concluded that the estimates of the number of periods of aberration per aperture which are based on rotating the spatial POD modes provide a better DM requirement than the estimations of the periods of aberration per aperture which are based on the original spatial POD modes. This conclusion is based on the observation that in Figure 13 (right), the number of periods of aberration per aperture in the spanwise direction is larger than the number of periods of aberration per aperture in the streamwise direction. This may indicated that the dominant, higher spatial frequencies, coherent structures propagate in the spanwise direction; however, as we already discussed above, the dominant, higher spatial frequencies, coherent structures propagate in the streamwise direction and not in the spanwise

direction. In addition, if we would compare the number of periods of aberration per aperture for the original spatial POD modes and the rotated spatial POD modes in both flow directions, we would conclude that based on the original POD modes, the number of periods of aberration per aperture are underestimated in the streamwise direction, and overestimated in the spanwise direction. Therefore, the correlation length should not be estimated based on the location of the original spatial POD modes, and the spatial POD modes should be rotated prior to calculating the correlation length.

5. CONCLUSION

The analysis techniques presented here for determining the two-dimensional velocity–distributions were shown to give the local convective velocity and the direction of convection over the aperture for a given look angle. These maps are helpful in characterizing the convective nature of the aberration field due to flow structures convecting over the aperture. They show, for example, potential locations of separation or reverse flow regions across the aperture and can identify cases where the flow is attached and the unsteadiness is due to stationary disturbances. So the method is helpful in understanding the basic character of the aberrations, and, knowing where separation pockets exist may be helpful in designing mitigation techniques using flow control.

Analysis of this type has been performed on copious in-flight AAOL wavefront data, and as long as the flow remains fully subsonic, the flow patterns once non-dimensionalized are virtually identical from one flight to the next as long as the same geometry turrets are used. So, in the presence or absence of flow control, this sort of information should be helpful in developing feed-forward type reconstruction algorithms for determining the DM figure to be applied in an adaptive-optic system to mitigate the deleterious aero-optic effects on the beam.

ACKNOWLEDGMENTS

REFERENCES

[1] Jumper, E. J., & Fitzgerald, E. J. (2001). Recent advances in aero-optics. *Progress in Aerospace Sciences, 37*(3), 299-339.
[2] Porter, C., Gordeyev, S., Zenk, M., & Jumper, E. J. (2011). Flight measurements of aero-optical distortions from a flat-windowed turret on the airborne aero-optics laboratory (AAOL). *42nd AIAA Plasmadynamics and Lasers Conference,* Honolulu, Hawaii. *, AIAA Paper 2011-3280.*
[3] Tyson, R. K. (1998). *Principles of adaptive optics* (2nd ed.). Boston: Academic Press.
[4] Rennie, R. M., Duffin, D. A., & Jumper, E. J. (2008). Characterization and aero-optic correction of a forced two-dimensional weakly compressible shear layer. *AIAA Journal, 46*(11), 2787-2795.
[5] Faghihi, A., Tesch, J., & Gibson, J. S. (2012). Identification, prediction, and control of aero-optical wavefronts. *Acquisition, Tracking, Pointing, and Laser Systems Technologies XXVI,* Baltimore, Maryland. *, SPIE Proceedings Vol. 8395.*
[6] Jumper, E. J., Gordeyev, S., Zenk, M., & Cavalieri, D. (2012). The airborne aero-optics laboratory (AAOL). *Acquisition, Tracking, Pointing, and Laser Systems Technologies XXVI,* Baltimore, Maryland. *, SPIE Proceedings Vol. 8395.*
[7] Goorskey, D. J. (2012). Spatial and temporal characterization of AAOL flight test data. *Acquisition, Tracking, Pointing, and Laser Systems Technologies XXVI,* Baltimore, Maryland. *, SPIE Proceedings Vol. 8395.*
[8] Whiteley, M. R., Goorskey, D. J., & Drye, R. (2012). Aero-optical jitter estimation using higher-order wavefronts. *Acquisition, Tracking, Pointing, and Laser Systems Technologies XXVI,* Baltimore, Maryland. *, SPIE Proceedings Vol. 8395.*
[9] Malley, M., Sutton, G. W., & Kincheloe, N. (1992). Beam-jitter measurements of turbulent aero-optical path differences. *Applied Optics, 31*(22), 4440-4443.

[10] Gordeyev, S., Hayden, T. E., & Jumper, E. J. (2004). Aero-optical and hot-wire measurements of the flow around the hemispherical turret with a flat window. *35th AIAA Plasmadynamics and Lasers Conference,* Portland, Oregon. *, AIAA Paper 2004-2450.*

[11] Gordeyev, S., Hayden, S., & Jumper, E. J. (2007). Aero-optical and flow measurements over a flat-windowed turret. *AIAA Journal, 45*(2), 347-347.

[12] Mathieu, J., & Scott, J. (2000). *An introduction to turbulent flow*. Cambridge New York: Cambridge University Press.

[13] Duffin, D. A., Gordeyev, S., & Jumper, E. J. (2004). Visualizing index-of-refraction variations in optically active flow fields. *11th International Symposium of Flow Visualization Conference,* Notre Dame, IN.

[14] Whiteley, M. R., & Goorskey, D. J. (2011). Influence of aero-optical disturbances on acquisition, tracking, and pointing performance characteristics in laser systems. *Acquisition, Tracking, Pointing, and Laser Systems Technologies XXV,* Orlando, Florida. *, SPIE Proceedings Vol. 8052.*

[15] Siegenthaler, J. P., Gordeyev, S., & Jumper, E. J. (2005). Shear layers and aperture effects for aero-optics. *36th AIAA Plasmadynamics and Lasers Conference,* Toronto, Canada. *, AIAA Paper 2005-4772.*

[16] DeLucca, N., Gordeyev, S., Jumper, E. J., Zenk, M., & Cavalieri, D.Recent data from the AAOL. *Acquisition, Tracking, Pointing, and Laser Systems Technologies XXVI,* Baltimore, Maryland. *, SPIE Proceedings Vol. 8395.*

[17] Gordeyev, S., & Jumper, E. J. (2010). Fluid dynamics and aero-optics of turrets. *Progress in Aerospace Sciences, 46*(8), 388-400.

[18] Chatterjee, A. (2000). An introduction to the proper orthogonal decomposition. *Current Science, 78*(7), 808-817.

[19] Proakis, J. G., & Manolakis, D. G. (1996). *Digital signal processing: Principles, algorithms, and applications* (3rd ed.). Upper Saddle River, New Jersey: Prentice Hall.

[20] Mela, K., & Louie, J. N. (2001). Correlation length and fractal dimension interpretation from seismic data using variograms and power spectra. *Geophysics, 66*(5), 1372-1378.

[21] Siegenthaler, J. P., Jumper, E. J., & Gordeyev, S. (2008). Atmospheric propagation vs. aero-optics. *46th AIAA Aerospace Sciences Meeting and Exhibit,* Reno, Nevada. *, AIAA Paper 2008-1076.*